

NRC Publications Archive Archives des publications du CNRC

Additively manufactured conformal cooling channels through topology optimization

Lamarche-Gagnon, Marc-Étienne; Molavi-Zarandi, Marjan; Raymond, Vincent; Ilinca, Florin

This publication could be one of several versions: author's original, accepted manuscript or the publisher's version. / La version de cette publication peut être l'une des suivantes : la version prépublication de l'auteur, la version acceptée du manuscrit ou la version de l'éditeur.

For the publisher's version, please access the DOI link below. / Pour consulter la version de l'éditeur, utilisez le lien DOI ci-dessous.

Publisher's version / Version de l'éditeur:

<https://doi.org/10.1007/s00158-024-03846-3>

Structural and Multidisciplinary Optimization, 67, 8, 2024-07-30

NRC Publications Archive Record / Notice des Archives des publications du CNRC :

<https://nrc-publications.canada.ca/eng/view/object/?id=f9bcb45a-9880-426c-895d-d54c8d88a8fe>

<https://publications-cnrc.canada.ca/fra/voir/objet/?id=f9bcb45a-9880-426c-895d-d54c8d88a8fe>

Access and use of this website and the material on it are subject to the Terms and Conditions set forth at

<https://nrc-publications.canada.ca/eng/copyright>

READ THESE TERMS AND CONDITIONS CAREFULLY BEFORE USING THIS WEBSITE.

L'accès à ce site Web et l'utilisation de son contenu sont assujettis aux conditions présentées dans le site

<https://publications-cnrc.canada.ca/fra/droits>

LISEZ CES CONDITIONS ATTENTIVEMENT AVANT D'UTILISER CE SITE WEB.

Questions? Contact the NRC Publications Archive team at

PublicationsArchive-ArchivesPublications@nrc-cnrc.gc.ca. If you wish to email the authors directly, please see the first page of the publication for their contact information.

Vous avez des questions? Nous pouvons vous aider. Pour communiquer directement avec un auteur, consultez la première page de la revue dans laquelle son article a été publié afin de trouver ses coordonnées. Si vous n'arrivez pas à les repérer, communiquez avec nous à PublicationsArchive-ArchivesPublications@nrc-cnrc.gc.ca.



Additively manufactured conformal cooling channels through topology optimization

Marc-Étienne Lamarche-Gagnon¹ · Marjan Molavi-Zarandi² · Vincent Raymond¹ · Florin Ilinca¹

Received: 22 December 2023 / Revised: 13 May 2024 / Accepted: 4 July 2024 / Published online: 30 July 2024
© Crown 2024

Abstract

Cooling channels play a critical role in various casting and molding processes, impacting both the cycle time and quality of the product. As additive manufacturing technologies become increasingly prevalent, conventional straight-drilled channels are being progressively substituted by intricate cooling lines that conform to the contours of the fabricated part. This transition can lead to a significant reduction of the solidification time and temperature gradients, consequently lowering the occurrence of part defects. However, designing such channels becomes challenging as geometric complexity and manufacturing constraints increase. In this work, we present a density-based topology optimization approach to generate conformal cooling channels in molds and dies inserts. To mitigate temperature variations, the objective function is penalized using the temperature standard deviation of the insert cavity surface. A density-gradient-based constraint is further utilized to reduce the generation of overhanging structures and promote manufacturability. In particular, the use of this constraint leads to the generation of channels characterized by a teardrop-shaped cross section. The cooling efficiency of a selected optimized design is confirmed through computations using a body-fitted solver. The geometry is subsequently manufactured by Laser Powder Bed Fusion (LPBF) and experiments are conducted to compare its performance in comparison to a design featuring straight-drilled channels. The results demonstrate that the optimized geometry significantly enhances the heat extraction rate and further leads to a 43% reduction of the cavity temperature standard deviation.

Keywords Topology optimization · Cooling channel · Additive manufacturing · Heat management

1 Introduction

Recently, there has been a conspicuous increase in the pursuit of enhanced efficiency of heat exchangers. This trend has not only impacted the heat exchanger sector but has also extended its reach into other domains, notably influencing the mold and die industry. A cooling channel design has a significant impact on the efficiency of heat exchangers and mold-die components in industrial processes (Feng et al.

2021). Cooling channels are typically drilled in straight lines, sometimes incorporating baffles and bubble, but these approaches often result in suboptimal cooling, particularly in areas prone to overheating. To achieve heightened levels of performance and sustainability, conformal cooling channels are a promising pathway for thermal management in temperature-dependent processes like aluminum die casting. These strategically positioned channels, however, cannot be achieved through traditional subtractive machining and necessitate the utilization of additive manufacturing (AM) techniques (Feng et al. 2021; Çalışkan et al. 2023).

Among the various AM processes, laser powder bed fusion (LPBF) stands out as one of the most common types, gaining significant attention from industries. The LPBF process constructs 3D objects by selectively melting a specific region of powdered particles on a layer-by-layer basis, following the design of a 3D model (Chowdhury et al. 2022). This unique manufacturing process makes LPBF a versatile technique that overcomes the challenges encountered by traditional manufacturing methods, thus

Responsible editor: Joe Alexandersen

✉ Marc-Étienne Lamarche-Gagnon
marc-etienne.lamarche-gagnon@nrc-cnrc.gc.ca

¹ Simulation and Numerical Modeling, Automotive and Surface Transportation Research Center, National Research Council Canada, Boucherville, QC J4B 6Y4, Canada

² Department of Mechanical Engineering & Engineering Science, The University of North Carolina at Charlotte, Charlotte, NC 28223, USA

enabling the manufacturing of complex cooling channels geometries. Central to the LPBF endeavor is the technique of topology optimization (TO). While TO has traditionally found its niche within structural design, it has the potential to spark transformative change in the realms of molds and dies through the creation of intricate cooling channel designs that match the shape of the mold cavity, thereby enhancing cooling consistency and the quality of the resulting products (Feng et al. 2021; Kanbur et al. 2020).

Currently, within the available categories of TO methods, there are three prominent general approaches: density, level-set, and homogenization methods. The former operates by assigning volume fraction (or “density”) values to regions within the design domain, translating into the presence or absence of a certain material or phase. Intermediate density values between 0 and 1 are commonly penalized to encourage a more binary (i.e., toward either 0 or 1) distribution of material (Sigmund and Maute 2013). Level-set TO employs a level-set function to represent the boundary separating the materials under consideration within the design domain. This method offers a crisp material transition compared to density-based methods. It allows for the creation of intricate shapes and is particularly well suited for shape and TO problems where complex geometry changes are involved (Van Dijk et al. 2013). Homogenization-based TO approaches consider both the macroscopic and microscopic scales of the material. They involve the analysis of how the microscale, represented by periodic geometric patterns, affects the overall behavior of the material and optimize its arrangement to achieve the desired performance characteristics (Wu et al. 2021).

Due to its remarkable capacity to provide extensive design flexibility, TO has been the subject of thorough research and has found applications in a wide array of domains. Borrvall and Petersson ((2003)) pioneered the study of fluid topology, which laid the foundation for subsequent multiphysics field coupling TO problems involving fluids. One of the early TO investigations addressing a conjugate heat transfer (CHT) problem (Dede 2009) proposed the design of a three-terminal heat sink via a gradient-based optimizer. Several CHT studies were subsequently conducted, exploring various variants of the canonical heat exchanger problem in two- (Koga et al. 2013; Matsumori et al. 2013; Qian and Dede 2016; Yaji et al. 2016; Qian et al. 2022; Wang et al. 2022) and three-dimensional (Yaji et al. 2015; Dilgen et al. 2018; Yu et al. 2020; Wang et al. 2023) contexts, and also natural convection problems (Alexandersen et al. 2016, 2018; Pollini et al. 2020; Li et al. 2022), among other applications.

To attain greater design flexibility and optimize LPBF manufacturability, additional advancements and refinements are essential. The literature often overlooks the geometric constraints inherent in metal additive manufacturing

methods when it comes to designing cooling channels. These constraints encompass aspects like build angles, where angles typically greater than 45° can function self-sufficiently and blend seamlessly into the design, while angles below this threshold usually lead to overhangs, which occur when the exposed layer exceeds the underlying one, and pose a considerable challenge without support material (Covarrubias and Eshraghi 2018; Garaigordobil et al. 2019). Channel diameter is another important consideration, as channels are typically self-supporting up to a certain diameter (Feng et al. 2021). A number of approaches have been employed to mitigate overhangs and generate self-supporting structures in TO. Gaynor and Guest (2016) proposed a formulation based on projection of design variables to ensure that all domain features are supported from the lower layers. Similarly, Langelaar (2017) developed the “layer-by-layer” filter approach, relying on the principle that material can only be placed if sufficiently supported from the layer below. van de Ven et al. (2018) extended the discrete layer-by-layer approach by modeling the AM printing process through a continuous front propagation strategy. The use of the build-plate-projection of the design variable gradient to identify overhanging regions within the domain was also proposed for density-based (Qian 2017) and level-set-based (Allaire et al. 2017; Wang et al. 2018; Miki 2023) approaches. For a comprehensive review of overhang-free methodologies, readers are directed to the work of Liu et al. (2018); Zhu et al. (2021); Ibhaddode et al. (2023).

Once the manufacturability of the optimized design is confirmed, a logical subsequent step involves experimental validation. To assess the performance of their design, Li et al. (2019a, b) subjected their prototype to a heat source while supplying a temperature-controlled fluid through the optimized channels. The authors used thermocouples and a thermal camera to validate their numerical simulations and quantify their design efficiency through pumping power and thermal resistance metrics. A similar apparatus was used by Zhan et al. (2023) in order to assess the performance based on the average temperature and pressure losses. The aforementioned experimental studies and several others used CNC-machined (Qian et al. 2022; Zhou et al. 2024) or AM (Ozguc et al. 2023; Sun et al. 2024) geometries closed by lids with simple planar external surfaces to replicate heat exchanger designs.

Despite the considerable effort dedicated to the design of heat exchangers through TO, only a limited amount of research has focused on conformal cooling systems within molds. Jahan et al. (2019) proposed a coupled thermal-fluid TO algorithm for the generation of conformal cooling channels for plastic injection molds. The design of conformal cooling lines for injection molding was also considered by Li et al. (2018) through the use of the channels’ diameters and positions as design variables. However, both studies

utilized a simplified modeling of the three-dimensional CHT problem. In the former, a planar CHT problem was considered and the ensuing conceptual design was transformed into a three-dimensional channel geometry, whereas the latter applied a boundary element approach to model both flow and heat transfer.

In this study, topology optimization is employed to generate conformal cooling channels in the context of heat management in a non-planar three-dimensional mold cooling system. The methodology relies on a density-based CHT approach and aims to maximize the heat extraction of a curved surface while ensuring a uniform temperature distribution. The latter is achieved by penalizing the cost function with the standard deviation (STD) of the surface temperature. As the geometry is intended to be manufactured by LPBF, our strategy further incorporates a modified projected-perimeter constraint (Qian 2017) to control the amount of overhangs in the domain. The optimized conformal cooling channel design is fabricated using LPBF and subjected to experimental testing, where its cooling performance is validated and compared to that of a conventional cooling system. Our study seeks to introduce a straightforward procedure for developing an integrated thermal–fluid methodology that streamlines the TO processes for cooling channel systems, while considering the constraints associated with LPBF additive manufacturing.

The article is structured as follows. The computational studies are presented in Sect. 2, first in terms of the adopted CHT modeling (Sect. 2.1) and finite element discretization (Sect. 2.2). The formulation of the optimization problem follows in Sect. 2.3 and results are shown in Sect. 2.4, highlighting the impact of employing the overhang constraint and STD penalization on the generated geometries. The validation of a selected design against a body-fitted solver is then presented in Sect. 2.5. Lastly, Sect. 3 exposes the experimental methodology and results, drawing comparisons with computational findings.

2 Computational studies

2.1 Governing equations

The methodology is developed in DFEMwork, a parallel and fully Distributed Finite Element Solver of the National Research Council of Canada. DFEMwork is implemented in C++ and utilizes distributed data structures and a single-program-multiple-data (SPMD) parallelism model with the MPI message passing standard. For details regarding the framework, concepts, and computational efficiency, we suggest referring to the research conducted by Audet et al. (2008).

The physical modeling is based on a conjugate heat transfer (CHT) problem for incompressible laminar flow in a pseudo-porous medium, and is governed by a set of steady-state conservation equations of mass, momentum, and energy. With the absence of gravitational force and neglecting pressure surface forces and viscous stresses in the energy conservation equation, the three equations can be expressed as follows:

$$\nabla \cdot \mathbf{u} = 0, \tag{1}$$

$$\rho \mathbf{u} \cdot \nabla \mathbf{u} + \nabla p - \nabla \cdot (\mu [\nabla \mathbf{u} + \nabla \mathbf{u}^t]) + C_\alpha (1 - \alpha) \mathbf{u} = 0, \tag{2}$$

$$\nabla \cdot (\rho c_p \mathbf{u} T) - \nabla \cdot (\kappa \nabla T) - q = 0, \tag{3}$$

where \mathbf{u} , p , T , and q , respectively, denote the velocity vector, pressure, temperature, and volumetric heat source and where ρ , μ , c_p , κ , and α designate the density, dynamic viscosity, heat capacity, thermal conductivity, and permeability, respectively. The body force $C_\alpha (1 - \alpha) \mathbf{u}$, hereafter termed the Darcy friction force, is added to the momentum equation to model the pseudo porosity of the medium and to enforce flow resistance in the non-fluid region ($\alpha < 1$). This term comprises the penalty parameter C_α . Note that the cancelation of the Darcy term in (2) results in a traditional CHT formulation, which assumes pure fluid and pure solid regions only; the latter problem will be referred to as *body-fitted*, as opposed to the *porous* formulation comprising the Darcy friction force.

The porosity of the medium is accounted for via the solid fraction, $\gamma(\mathbf{x})$, a continuous scalar field that quantifies the local proportion of solid and varies from 0 (full fluid) to 1 (full solid). The thermal conductivity κ and permeability α are linked to the solid fraction via Rational Approximation of Material Properties (RAMP) interpolation schemes (Stolpe and Svanberg 2001a), expressed as

$$\kappa := \kappa_{\text{fluid}} + (\kappa_{\text{solid}} - \kappa_{\text{fluid}}) \frac{\gamma}{1 + P_\kappa (1 - \gamma)}, \tag{4}$$

$$\alpha := \alpha_{\text{fluid}} + (\alpha_{\text{solid}} - \alpha_{\text{fluid}}) \frac{\gamma}{1 + P_\alpha (1 - \gamma)}, \tag{5}$$

where the fluid and solid subscripts refer to the corresponding state value for the thermal conductivity, while $\alpha_{\text{fluid}} = 1$ and $\alpha_{\text{solid}} = 0$. P_κ and P_α are two penalty coefficients, generally set to values greater than one in order to penalize intermediate solid fraction values in the optimization problem, while avoiding excessively large penalizations to prevent a premature convergence to local minima (Sigmund and Maute 2013). In this work, the coefficients are assigned to $P_\kappa = 4$ and $P_\alpha = 400$ following a preliminary comparison of the porous temperature

and velocity solutions versus the body-fitted solver (see Sect. 2.5). Lastly, since velocity magnitudes in the solid regions are orders of magnitude lower than in the bulk fluid, the density, heat capacity, and viscosity of the solid state have a negligible influence in (2) and (3); hence, these quantities are not interpolated, but set to the corresponding fluid value.

2.2 Finite element formulation

The formulation employed in this study is based on a discretization of the geometry using linear tetrahedron elements. The governing partial differential equations (1)–(3) are converted to variational residual formulations, R^k , with $k \in [0..4]$, and are solved following a Galerkin/least-squares (GLS) approach (Tezduyar et al. 1992). The mass ($k = 0$) and momentum ($k \in [1..3]$) residual equations can be found in our previous work (Navah et al. 2024), but are also provided in the following for completion, viz.

$$R^0 := \int_{\Omega} \varphi^k \nabla \cdot \mathbf{u} \, d\Omega + \sum_K \int_{\Omega_K} \tau_u \nabla \varphi^k \cdot \mathbf{r}_u \, d\Omega = 0, \tag{6}$$

$$\begin{aligned} \begin{bmatrix} R^1 \\ R^2 \\ R^3 \end{bmatrix} &:= \int_{\Omega} [\varphi^k \rho \mathbf{u} \cdot \nabla \mathbf{u} - p \nabla \varphi^k + \mu \nabla \varphi^k \cdot (\nabla \mathbf{u} + \nabla \mathbf{u}^t)] \\ &+ \varphi^k C_{\alpha} (1 - \alpha) \mathbf{u} \, d\Omega + \sum_K \int_{\Omega_K} \rho \tau_u \mathbf{u} \cdot \nabla \varphi^k \mathbf{r}_u \, d\Omega \\ &- \int_{\Gamma_{NS}} \varphi^k (\mu [\nabla \mathbf{u} + \nabla \mathbf{u}^t] \cdot \mathbf{n} - pn) \, d\Gamma = 0, \end{aligned} \tag{7}$$

where φ^k designates the test function for equation k , τ_u denotes the velocity stabilization parameter (Navah et al. 2024), \mathbf{n} is the outward normal unit vector on Γ_{NS} , the boundary of the domain where Neumann conditions are applied for the Navier–Stokes equations, and where

$$\mathbf{r}_u = \rho \mathbf{u} \cdot \nabla \mathbf{u} + \nabla p - \nabla \cdot (\mu [\nabla \mathbf{u} + (\nabla \mathbf{u})^t]) + C_{\alpha} (1 - \alpha) \mathbf{u} \tag{8}$$

is the strong residual vector of the momentum equations. In order to enforce global energy conservation within the system, the energy equation is solved in its conservative form, contrary to the approach in our previous work (Navah et al. 2022, 2024). For constant density and heat capacity, this translates into

$$\begin{aligned} R^4 &:= \int_{\Omega} \varphi^k [\rho c_p (\mathbf{u} \cdot \nabla T + T \nabla \cdot \mathbf{u}) - q] + \kappa \nabla T \cdot \nabla \varphi^k \, d\Omega \\ &+ \sum_K \int_{\Omega_K} \rho c_p \tau_T \mathbf{u} \cdot \nabla \varphi^k [\rho c_p \mathbf{u} \cdot \nabla T - \nabla \cdot (\kappa \nabla T) - q] \, d\Omega \\ &+ \sum_K \int_{\Omega_K} \rho c_p \tau_u T \nabla \varphi^k \cdot \mathbf{r}_u \, d\Omega \\ &- \int_{\Gamma_E} \varphi^k \kappa \nabla T \cdot \mathbf{n} \, d\Gamma = 0, \end{aligned} \tag{9}$$

where Γ_E is the boundary of the domain where Neumann conditions are applied, τ_T is the stabilization parameter of the equation of energy (Navah et al. 2024), and the third line of (9) contains the terms arising from the stabilization of the velocity divergence, needed in the conservative form.

Since the main objective of this study is optimal thermal management, it is crucial to adopt proper measures to minimize sources of error in the heat transfer solution. Preliminary computations revealed that neglecting the term $T \nabla \cdot \mathbf{u}$ in (9) can lead to heat balance errors exceeding 15% in the considered CHT problems, although the error diminished as the mesh was refined. This can be explained by the finite element formulation not enforcing strict local (at the element level) mass conservation, consequently impacting energy conservation. As the adoption of the conservative form reduces the heat balance error by several orders of magnitudes, it is considered to be negligible in this work. Heat balance verification is a frequently overlooked aspect in the literature and warrants careful consideration.

2.3 Optimization problem and methods

The topology optimization problem solved in this study is formulated as follows:

$$\begin{aligned} \min_{\hat{\gamma}} \quad &\mathcal{C}(\gamma, p(\gamma), \mathbf{u}(\gamma), T(\gamma)), \\ \text{s.t.} \quad &\mathcal{G}_i(\hat{\gamma}) \leq 0, \quad i \in [1..N_G], \\ &R^k(\gamma, p(\gamma), \mathbf{u}(\gamma), T(\gamma)), \quad k \in [0..4], \\ &\hat{\gamma}_{\min} \leq \hat{\gamma} \leq \hat{\gamma}_{\max}, \end{aligned} \tag{10}$$

where $\hat{\gamma}$, \mathcal{C} , and \mathcal{G}_i stand for the design variable, the cost function, and the i^{th} (out of N_G) inequality constraint, respectively, while R^k denotes the system of discrete residual equations arising from the k th partial differential equation of (1)–(3). All equations are solved for given solid fraction field γ , the later of which is a result of a three-field projection of the design variable. The first step consists of a typical density filtering scheme (Bruns and Tortorelli 2001; Sigmund 2007), here defined as

$$\tilde{\gamma} := \mathcal{D} \hat{\gamma}, \tag{11}$$

where $\mathcal{D}_{ij} := \omega_{ij} v_j / \sum_{k \in \mathcal{N}_i} \omega_{ik} v_k$ is a sparse matrix having non-zero values for $j \in \mathcal{N}_i$, with \mathcal{N}_i the set of nodes within the sphere of radius ρ and centered on \mathbf{x}_i , $\omega_{ij} := \rho - \|\mathbf{x}_i - \mathbf{x}_j\|$, and v_j is the nodal weight for node j (Navah et al. 2024). The filtering step is then followed by a smoothed Heaviside projection (Wang et al. 2011), expressed as

$$\gamma := \frac{\tanh(\beta\eta) + \tanh(\beta(\tilde{\gamma} - \eta))}{\tanh(\beta\eta) + \tanh(\beta(1 - \eta))}, \tag{12}$$

where β is a sharpness parameter and η denotes the threshold value. γ is also commonly referred to as the ‘‘physical’’ design variable in the literature, given that it is the variable considered in the residual equations. The optimization problem bounds are fixed to $\hat{\gamma}_{\min} = 0$ and $\hat{\gamma}_{\max} = 1$.

2.3.1 Cost function and constraints

The objective of the proposed topology optimization formulation is the design of cooling channels in molds, which are to be manufactured by additive manufacturing (LPBF). As in most heat transfer applications, maximal heat extraction is desired, which is here formulated as the minimization of the surface temperature of the insert cavity considering the use of a heat flux boundary condition for the cavity surface. Furthermore, temperature uniformity during the cooling phase is another crucial aspect in many casting applications, as too large temperature gradients throughout the part can lead to higher residual stresses and part deflections (Mazur et al. 2017; Kanbur et al. 2020; Feng et al. 2021). Consequently, a penalization on the cavity temperature standard deviation (STD), σ_c , is employed in this work. The latter strategy is preferred, in our context, to other approaches such as the minimization of the maximal temperature (through the use of e.g., the temperature p -norm, $p > 1$ Zhang and Liu 2008), as the latter do not directly penalize low-temperature (or over-cooled) regions, which are also undesirable. Finally, the cost function is further penalized by the inlet-to-outlet pressure drop, $\Delta p_{\text{in-out}}$, in order to promote the generation of channels and is thus expressed as

$$\mathcal{C} := \bar{T}_c + \lambda_p \Delta p_{\text{in-out}} + \lambda_\sigma \sigma_c, \tag{13}$$

where \bar{T}_c denotes the surface-averaged temperature of the cavity, while λ_p and λ_σ stand for the pressure drop and temperature STD penalty coefficients, respectively. The $\Delta p_{\text{in-out}}$ and σ_c penalization terms are computed as

$$\Delta p_{\text{in-out}} := \frac{\int_{\Gamma_{\text{in}}} p \, d\Gamma}{\int_{\Gamma_{\text{in}}} d\Gamma}, \tag{14}$$

and

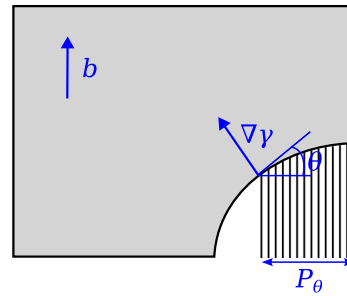


Fig. 1 Projected perimeter \mathcal{P}_θ

$$\sigma_c := \sqrt{\frac{\int_{\Gamma_c} (T - \bar{T}_c)^2 \, d\Gamma}{\int_{\Gamma_c} d\Gamma}} \tag{15}$$

$$= \sqrt{\frac{\int_{\Gamma_c} T^2 \, d\Gamma}{\int_{\Gamma_c} d\Gamma} - \bar{T}_c^2} \tag{16}$$

where Γ_{in} and Γ_c , respectively, refer to the inlet and cavity boundaries. As the outlet pressure is set to zero, $\Delta p_{\text{in-out}}$ equals to the inlet value. One will further note that (16), which leverages the fact that \bar{T}_c is an averaged value, is favored over (15) for its computational efficiency.

Two constraints ($N_G = 2$) are considered in this work. The first consists in constraining the maximal volume of fluid and is expressed as

$$\mathcal{G}_1 := 1 - \bar{\gamma} \leq 1 - \bar{\gamma}_0, \tag{17}$$

with $\bar{\gamma} := \int_{\Omega} \gamma(\mathbf{x}) \, d\Omega / \int_{\Omega} d\Omega$ the total (same as average) solid fraction value and $\bar{\gamma}_0$ a user-defined value. Because the optimized cooling channel design is intended to be additively manufactured, the second constraint aims at preventing the formation of overhanging structures. The latter is formulated as a modified version of the projected-perimeter constraint proposed by Qian (2017), viz.

$$\mathcal{G}_2 := \mathcal{P}_\theta \leq \mathcal{P}_0, \tag{18}$$

$$\mathcal{P}_\theta := \int_{\Omega} \mathcal{H}\left(\mathbf{b} \cdot \frac{\nabla \tilde{\gamma}}{\|\nabla \tilde{\gamma}\|} - \cos \theta\right) \mathbf{b} \cdot \nabla \tilde{\gamma} \, d\Omega, \tag{19}$$

where \mathcal{P}_0 is the maximal allowed projected perimeter, \mathbf{b} designates the build direction, θ denotes the overhang angle, and \mathcal{H} is an Heaviside projection, defined as

$$\mathcal{H}(\xi) := (1 + \exp(-2\beta_\theta \xi))^{-1}, \tag{20}$$

with β_θ a parameter controlling the smoothness of the transition to 0–1 values. For $\beta_\theta \rightarrow \infty$, the projection is

non-zero for $\mathbf{b} \cdot \frac{\nabla \tilde{\gamma}}{\|\nabla \tilde{\gamma}\|} \geq \cos \theta$; (19) thus penalizes regions where the angle between $\nabla \tilde{\gamma}$ and \mathbf{b} is lower than θ , as exposed in Fig. 1. For the current optimization context, this constraint can prevent the generation of channels with a flat top surface.

In this work, the original projected-perimeter formulation is modified by using the filtered design variable, $\tilde{\gamma}$, in (19) instead of the physical design variable, γ . This change is motivated by the observation that, for a crisp γ distribution, the discrepancies between the $\gamma \approx 0.5$ and $\tilde{\gamma} \approx 0.5$ isosurfaces are, in general, small, except for the much smoother definition of the latter (see Appendix A). Consequently, the $\tilde{\gamma}$ field can be utilized to generate the body-fitted mesh without causing a substantial change in the design efficiency, which makes $\tilde{\gamma}$ a logical choice for the projected-perimeter formulation. The effectiveness of this adjustment will be demonstrated in Sect. 2.4.3. Lastly, a value of 10 is utilized for β_θ (as in the original paper Qian 2017), $\theta = 45^\circ$ and $\mathbf{b} = (0, 0, 1)$.

2.3.2 Methodology

In order to avoid premature convergence to local minima and decrease the sensitivity to the initial design (Sigmund and Maute 2013; Stolpe and Svanberg 2001b), a continuation approach is employed, which consists of progressively increasing selected hyper-parameters through a series of optimization loops. The definition of the strategy depends strongly on the physical problem(s) being solved and on the parametrization utilized. To the authors' knowledge, there are no specific guidelines regarding which parameter should be increased first, and which one should be fixed. Drawing from experience, the following strategy, comprising a total of 12 optimization loops, is adopted:

1. For loop $i_{loop} \in [0..6]$, increase the Heaviside projection coefficient, β , from 1 to 64 following $\beta = 2^{i_{loop}}$, with fixed $C_\alpha = 1 \times 10^6$;
2. For loop $i_{loop} \in [7..11]$, increase the Darcy penalty factor following the list $C_\alpha \in [3 \times 10^6, 1 \times 10^7, 3 \times 10^7, 1 \times 10^8, 3 \times 10^8]$, with fixed $\beta = 64$.

We noticed that starting with a low C_α resulted in a smoother overall convergence (see Appendix B). For all loops, the fixed hyper-parameters are as follows: $P_\kappa = 4$, $P_\alpha = 400$, $1 - \tilde{\gamma}_0 = 0.05$, $\rho = 0.003$, $\eta = 0.5$, and $\lambda_p = 1$. λ_σ and \mathcal{P}_0 are also fixed to case-dependent values (see Sect. 2.4). Each optimization loop is stopped if the relative cost function difference between consecutive steps is lower than 10^{-5} , with

a maximum of 100 optimization steps. Operations executed within each step are as follows:

1. Projection of the design variable, $\hat{\gamma} \rightarrow \tilde{\gamma} \rightarrow \gamma$, using (11) and (12);
2. Resolution of the system of residual state Eqs. (6), (7), and (9);
3. Evaluation of the cost function \mathcal{C} and constraints \mathcal{G}_i using (13), (17) and (18);
4. Computation of the sensitivities $\frac{d\mathcal{C}}{d\hat{\gamma}}$ and $\frac{d\mathcal{G}_i}{d\hat{\gamma}}$ following an adjoint-based approach (see Sect. 2.3.3);
5. Update of $\hat{\gamma}$ using the Method of Moving Asymptotes (MMA, Svanberg 1987), with a move limit of 0.05.

2.3.3 Sensitivities

As our approach is gradient-based, the cost function (and constraints) derivative with respect to the design variable must be provided to the optimizer. Following an adjoint-based approach, the cost function gradient with respect to the solid fraction can be expressed as (Navah et al. 2024)

$$\frac{d\mathcal{C}}{d\gamma} = \frac{\partial \mathcal{C}}{\partial \gamma} + \lambda^{NS\top} \frac{\partial \mathbf{R}^{NS}}{\partial \gamma} + \lambda^E \frac{\partial \mathbf{R}^E}{\partial \gamma}, \tag{21}$$

where λ^{NS} and λ^E are the adjoint variables obtained following the successive resolutions of the two sets of adjoint equations, viz.

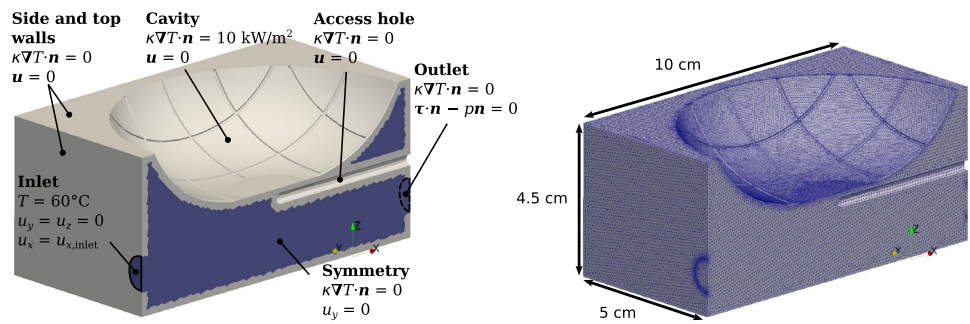
$$\left(\frac{\partial \mathbf{R}^E}{\partial T} \right)^\top \lambda^E = - \left(\frac{\partial \mathcal{C}}{\partial T} \right)^\top, \tag{22}$$

$$\left(\frac{\partial \mathbf{R}^{NS}}{\partial \mathbf{U}^{NS}} \right)^\top \lambda^{NS} = - \left(\frac{\partial \mathbf{R}^E}{\partial \mathbf{U}^{NS}} \right)^\top \lambda^E - \left(\frac{\partial \mathcal{C}}{\partial \mathbf{U}^{NS}} \right)^\top, \tag{23}$$

where $\mathbf{R}^E := R^4$ and $\mathbf{R}^{NS} := [R^0, R^1, R^2, R^3]$, respectively, stand for the energy and Navier–Stokes residual equations and $\mathbf{U}^{NS} := [p, u_x, u_y, u_z]$. In this work, all jacobian matrices are evaluated via numerical differentiation, while $\partial \mathcal{C} / \partial T$ and $\partial \mathcal{C} / \partial \mathbf{U}^{NS}$ are computed analytically (see Appendix C) and $\partial \mathcal{C} / \partial \gamma = 0$. As the constraints sensitivities, $\frac{d\mathcal{G}_1}{d\gamma}$ and $\frac{d\mathcal{G}_2}{d\gamma}$, only depend on γ (and not on the state variables T and \mathbf{u}), their analytical derivations are straightforward.

Finally, the sensitivities with respect to the design variable $\hat{\gamma}$ are evaluated via the chain rule (Sigmund 2007; Navah et al. 2024).

Fig. 2 Left: optimization domain and boundary conditions. The blue region denotes the design domain, whereas the gray nodes are fixed to solid ($\gamma = 1$). Right: external dimensions and computational mesh



2.4 Optimization cases

2.4.1 Geometry and conditions

The computational domain and mesh considered for the optimizations are displayed in Fig. 2, along with the imposed boundary conditions. The cuboid domain comprises a hemispherical-like cavity on its top, circular inlet and outlet of diameter $d = 1$ cm on either y - z side along with a cylindrical hole (referred to as “access hole”) of diameter 0.318 cm and length 5 cm for probing access. Small grooves are added to the cavity surface to facilitate visual inspection of the temperature distribution in the experiments. Because of geometrical symmetry, only half of the domain is considered for the computations. The computational mesh is generated using Gmsh (Geuzaine and Remacle 2009) and comprises 1.67×10^5 nodes (9.93×10^5 elements).

Water at a temperature of 60°C ¹ enters the domain with a parabolic velocity profile, $u_{x,\text{inlet}}$, of maximum velocity 0.171 m/s. The outlet is set free for \mathbf{u} and T . No-slip and adiabatic conditions are applied to all other boundaries, except for the cavity, where the adiabatic condition is replaced by a heating flux of 10 kW/m^2 , and for the symmetry boundary, where the no-slip condition is applied in the y direction only, while the other two velocity components are set free. The initial material distribution is $\gamma = 1$, i.e., fully solid. The thermofluid properties correspond to those of water and maraging steel (18Ni-300) and are set to $\rho = 997 \text{ kg/m}^3$, $c_p = 4200 \text{ J/kg}\cdot\text{K}$, $\mu = 8.5 \times 10^{-4} \text{ N}\cdot\text{s/m}^2$, $\kappa_{\text{fluid}} = 0.6 \text{ W/m}\cdot\text{K}$, and $\kappa_{\text{solid}} = 16 \text{ W/m}\cdot\text{K}$, corresponding to inlet Reynolds and Prandtl numbers of 1003 and 5.95, respectively. The Darcy number based on the inlet diameter and final C_α value, $\text{Da} = \mu / (C_{\alpha,\text{max}} d^2)$, is 2.8×10^{-8} . Phase change of water, in regions where the local temperature exceeds the boiling condition, is not considered in this work. It is further worth noting, thanks to the linearity of the energy conservation equation, that any changes in the

heat flux or inlet temperature value, accompanied by a corresponding adjustment of the penalty parameters, will result in the same optimal design being reached.

All nodes within a normal distance of 0.2 cm from the side and top walls, cavity, and access hole boundaries were fixed to solid ($\gamma = 1$, see Fig. 2) to ensure structural integrity and watertightness of the generated optimized channel designs.

Computations are carried on NRC’s computer cluster using four Xeon Gold 6126 processors, which amounts to a total of 48 cores. For Case D, the average computational times per optimization step for solving the states equations and computing the sensitivities are 11.2 s and 4.3 s, respectively. The observed times for the other cases are within 10% of these values.

2.4.2 Results

To investigate the impact of the STD penalization and overhang constraint, four optimization cases are first considered, the parameters of which are presented in Table 1: Case A is the baseline example, where \mathcal{G}_2 is deactivated and $\lambda_\sigma = 0$. Next, Cases B and C are selected to explore the isolated impacts of the STD penalization and overhang constraint, while Case D considers both effects. The values of $\lambda_\sigma = 10$ and $\mathcal{P}_0 = 2$ were chosen following a preliminary calibration exercise, where each parameter was varied over a range of values.

The final design for Cases A–D is shown in Fig. 3, along with the temperature distribution of the cavity and top surfaces. A first observation is that, as expected, the cavity temperature is much more uniform for Cases B and D, i.e., when the STD penalization is utilized. Indeed, Table 2 shows that σ_c is over six and ten times lower for the respective Cases B and D, in comparison to the baseline result. The lower thermal gradients can be mostly attributed to the

Table 1 Optimization cases and their hyper-parameters

Case	A	B	C	D	E	F
λ_σ	0	10	0	10	10	10
\mathcal{P}_0	–	–	2	2	5.2	3.5

¹ This relatively high value is selected in accordance with industrial practices to prevent issues such as excessive cooling, which can lead to overly large thermal gradients and stresses.

Fig. 3 Final design (left), as represented by a clip on $\tilde{\gamma} \leq 0.5$ and mirrored along the $y = 0$ plane, and top view of the temperature solution (right) for Cases A–D. (Color figure online)

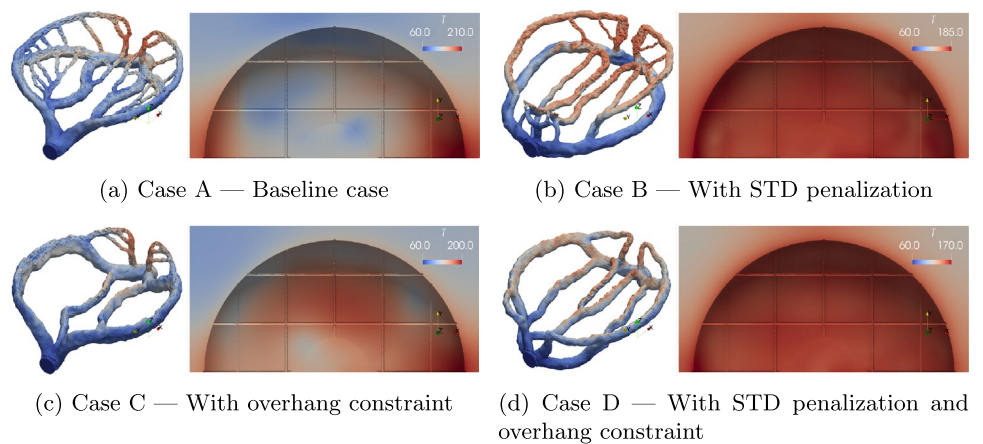


Table 2 Selected metrics for the final optimization designs

Case	A	B	C	D	E	F
\bar{T}_c (C)	145.8	173.1	156.2	158.5	147.9	150.6
σ_c (C)	22.9	3.52	15.7	2.02	2.07	3.42
Δp_{in-out} (Pa)	70.7	124.9	64.4	105.1	111.7	156.5
\mathcal{C} (C)	216.4	333.1	220.7	283.9	280.3	341.3
Discreteness (%)	2.88	3.27	2.48	2.87	3.05	3.36
$1 - \bar{\gamma}$ (-)	0.500	0.500	0.500	0.500	0.500	0.500
$\mathcal{P}_\theta, \mathcal{P}_\theta^*$ (-)	7.93	9.86	2.01	2.01	5.21	3.50

The level of discreteness is computed as $\int_\Omega 4\gamma(1 - \gamma) d\Omega / \int_\Omega d\Omega$ (Sigmund 2007). Values in the bottom line correspond to \mathcal{P}_θ for Cases A–D and to \mathcal{P}_θ^* for Cases E–F

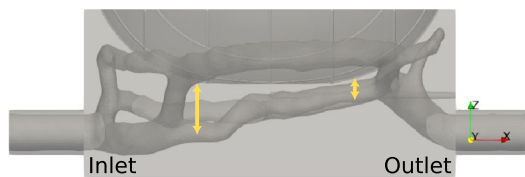


Fig. 4 Side view of the final design for Case D, highlighting the streamwise variation of the channel-to-cavity distance

streamwise variation of the channel-to-cavity distance: as depicted by Fig. 4 for Case D, this distance is larger near the inlet, where the fluid is colder, and decreases toward the outlet to compensate for the heating of the fluid. For Case B (Case D), the improved uniformity comes at the cost of a 19% (8.8%) increase of the average cavity temperature and a 77% (49%) rise in Δp_{in-out} . Figure 3 further shows that the activation of the overhang constraint (Cases C and D) leads to channels more elongated along the build direction (z). From the cut view of Fig. 5b, it can be seen that this constraint tends to generate teardrop-shaped cross sections, as also reported by the work of Behrou et al. (2022) which employed a projection-based overhang-limiting approach. Another consequence of the use of \mathcal{G}_2 is the generation of fewer parallel channels of larger cross section. This can be

attributed to the conjecture that higher pressure losses are observed in teardrop-shaped channels. To compensate for these losses, and in order to satisfy both volume and overhang constraints, the optimizer is compelled to produce a smaller number of channels with larger cross sections. It is worth noting that this adjustment also leads to a decrease in Δp_{in-out} for Cases C and D when compared to Cases A and B, respectively, although this consequence should not be generalized and may be specific to these particular cases. An additional interesting observation is that, despite Case B being less constrained than Case D, it exhibits higher values for both σ_c and \bar{T}_c . One could speculate that the specific set of chosen hyper-parameters has resulted in Case B converging to a suboptimal local minimum. It is reasonable to anticipate further improvements on σ_c and \bar{T}_c with finer tuning, although this may also lead to a poorer performance for the other cases.

In geometries with heated surfaces, topology optimized channels tend to come in contact with the heat source as the Reynolds number increases (Navah et al. 2024), sometimes leading to the formation of flat or thin channel strips. While this may be efficient for heat extraction, it can be undesirable from a LPBF manufacturing point of view. This behavior is particularly evident for Case A, where, as Figs. 5a and 6a show, many channels are in contact with the cavity-side boundary

Fig. 5 Channels cross section along the $x = 0$ (mid-distance between the inlet and outlet) plane

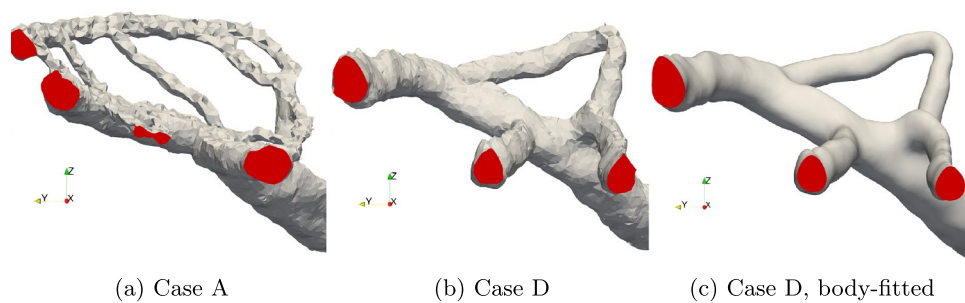


Fig. 6 Enlarged view of the final design for Cases A and D, along with the $y = -0.025$ plane colored blue for nodes within the design domain. The distance separating the channels and design domain boundary is highlighted in specific regions with yellow markings. (Color figure online)

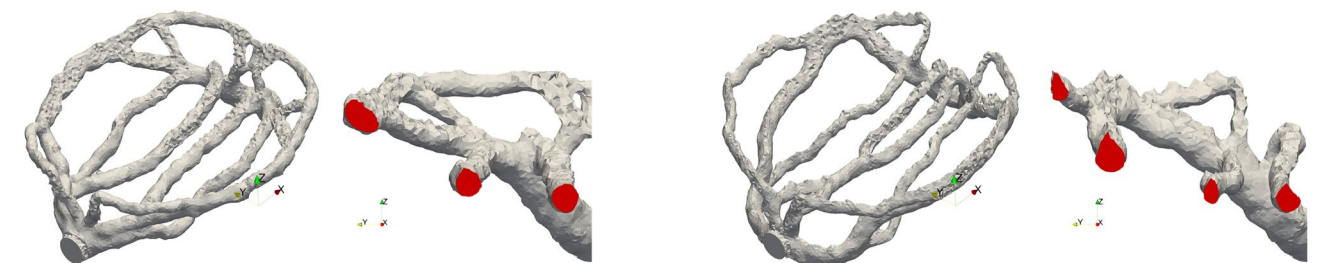
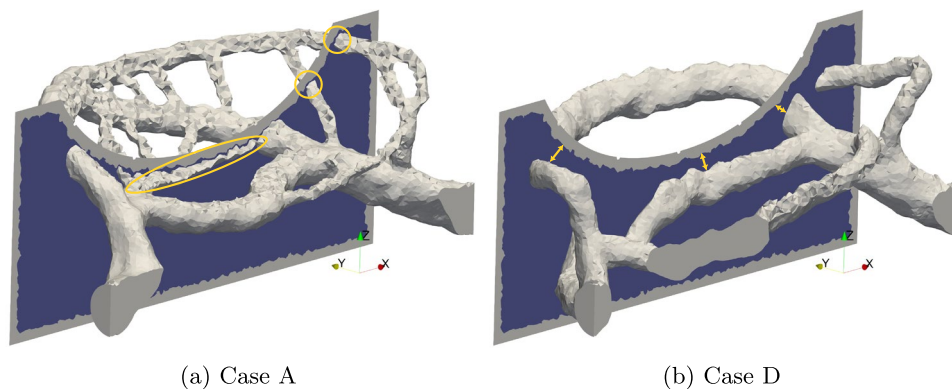


Fig. 7 Optimized design (mirrored along the $y = 0$ plane) and channels cross section on the $x = 0$ plane for Cases E (left) and F (right)

of the design domain; this also explains the jagged channel surfaces in this region, which are a result of the mesh resolution. In contrast, when activating the overhang constraint, the generation of channels of flat top surface is prevented. When further including the STD penalization, channels tend to form slightly farther away from the heated cavity to prevent overcooling, as observed in Fig. 6b.

2.4.3 Comparison with the original projected-perimeter formulation

Computations are now performed using the original projected-perimeter formulation (as proposed by Qian 2017), i.e., by replacing $\tilde{\gamma}$ with γ in (19), viz.

$$\mathcal{P}_\theta^* := \int_\Omega \mathcal{H}\left(\mathbf{b} \cdot \frac{\nabla\gamma}{\|\nabla\gamma\|} - \cos\theta\right) \mathbf{b} \cdot \nabla\gamma \, d\Omega, \tag{24}$$

and by further setting $\mathcal{G}_2 := \mathcal{P}_\theta^* < \mathcal{P}_0$ and $\lambda_\sigma = 10$. Two values for \mathcal{P}_0 are used: (i) \mathcal{P}_θ^* evaluated on the final design of Case D and (ii) 65% of that value, corresponding to the conditions of Cases E and F, respectively. The main results are provided in Table 2 and Fig. 7 and can be summarized as follows. The cost function for Case E is roughly 1% lower than for Case D, explained mainly by a slightly lower \bar{T}_c , but higher Δp_{in-out} . However, a visual inspection of the final design shows a higher degree of overhanging regions, i.e., where the top wall of channels tends to be flat. Reducing \mathcal{P}_0 to 3.5 (Case F) effectively eliminates most overhangs, but comes at the expense of a significantly higher \mathcal{C} compared to Case D. The increased cost is primarily due to a

Fig. 8 Body-fitted mesh cut view (left) and fluid region (right)

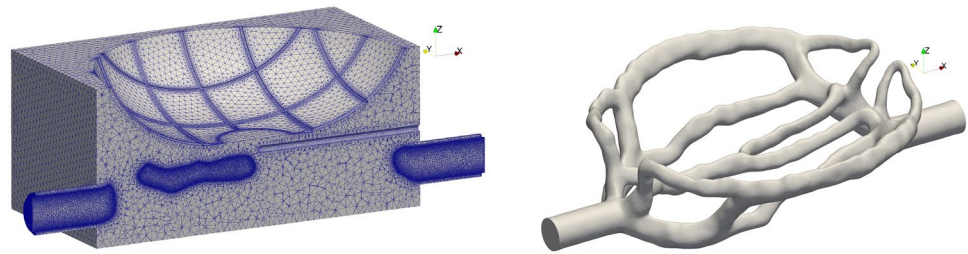
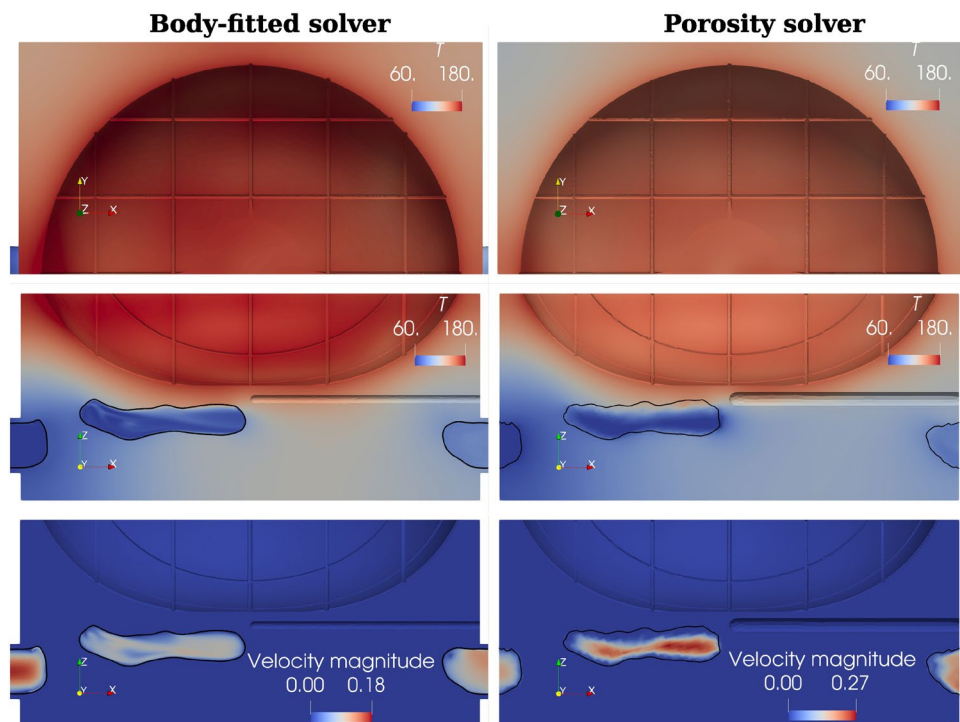


Table 3 Body-fitted and porous solution results

Case	N_{ele}	\bar{T}_c (C)	σ_c (C)	$\Delta p_{\text{in-out}}$ (Pa)
Body-fitted	3.72×10^7	171.91	4.75	17.47
Porous	9.93×10^5	158.51	2.02	105.10
Porous, $\uparrow P_\kappa \uparrow P_\alpha$	9.93×10^5	164.79	5.17	19.64

Fig. 9 Body-fitted (left) and porosity (right) solvers, temperature, and velocity magnitude solutions—top and cut (along the $y = 0$ plane) views. The solid black lines in the cut views correspond to the solid-to-fluid interface (left) and $\tilde{\gamma} = 0.5$ isocontour (right)



1.5-fold rise in $\Delta p_{\text{in-out}}$ and a 1.7-fold increase in σ_c . Hence, to obtain a design with an acceptable level of overhangs, \mathcal{P}_0 has to be set to a more aggressive value, which restrains the design space and leads to a lower final design efficiency. We conjecture that this behavior is explained by the induced roughness of the implicit surface representation using γ (see e.g., Fig. 17), which increases the total projected perimeter.

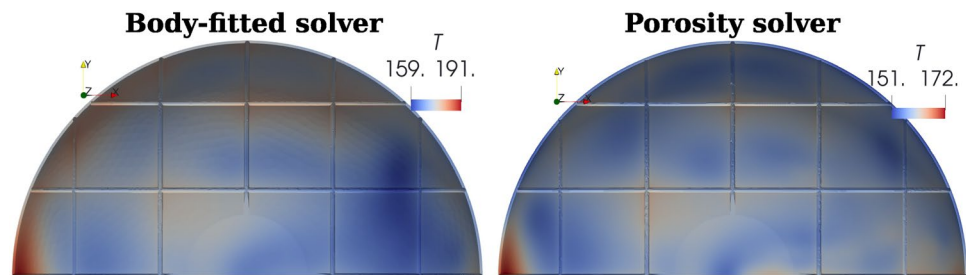
² A value slightly larger than 0.5 is used to compensate for design shrinking resulting from the filtering steps.

2.5 Validation

The central focus of this study is to develop a heat management system for a die casting insert. Therefore, the subsequent analyses only consider the design from Case D, as the latter incorporates LPBF manufacturing considerations and minimizes temperature gradients on the cavity surface.

The body-fitted mesh for Case D is generated by first splitting the mesh on the $\tilde{\gamma} = 0.55^2$ isosurface using the mmg3d library (Dapogny et al. 2014). Next, the fluid-to-solid interface is mirrored and imported, as a STL file, into

Fig. 10 Body-fitted vs. porosity solvers temperature—focus on the cavity



the Meshlab software (Cignoni et al. 2008), where it is remeshed with uniform-size triangles and smoothed using the Taubin algorithm. The channels are then recombined into the cuboid domain using Meshlab’s boolean operations, along with the addition of inlet and outlet ports. Finally, the whole domain is meshed with tetrahedral elements using Gmsh; the maximum element size and element growth rate are made smaller in the fluid region. The resulting mesh has 5.56×10^6 nodes (3.72×10^7 elements), namely more than 37 times the number of elements of the porous mesh (half domain). The mesh density was selected following a grid convergence study, where a twofold increase of the minimal fluid element size (resulting in 8.43×10^6 elements in total) leads to a difference of 0.3% on $\Delta p_{\text{in-out}}$. Figure 8 provides a cut view of the mesh and displays the smoothed channels design. The impact of the smoothing operation on the channels and their cross section can further be visualized in Fig. 5c.

The body-fitted mesh is next utilized to solve the Navier–Stokes and energy conservation equations using the body-fitted solver under the conditions of Case D. We recall that the body-fitted formulation is equivalent to the porous CHT problem (see Sect. 2.1) with the Darcy term canceled out; consequently, the Navier–Stokes equations are only solved within the fluid subdomain. As observed in Fig. 9, the body-fitted and porous temperature distributions exhibit fair agreement, although temperatures in the vicinity of the cavity are slightly lower for the porous solution; \bar{T}_c is indeed about 10 degrees lower for the latter (see Table 3).

³ By effective channel diameter, we refer to the cross-section size based on the $\|\mathbf{u}\| \rightarrow 0$ isosurface, corresponding to the extent of the fluid boundary layer.

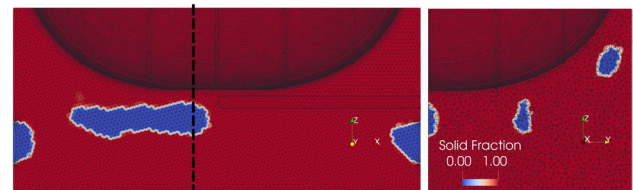


Fig. 11 Solid fraction distributions depicted from a y-normal perspective (left) and a cut view (right) along the dashed line, overlaid with the mesh elements

Furthermore, from the focused view of the cavity plotted in Fig. 10, it can be seen that the body-fitted solution shows more variations. In particular, the region toward the outlet is slightly over-cooled, resulting in a cavity temperature STD about 2.5 times higher than the corresponding porous solution value. Despite these differences, the STD value for the body-fitted solution remains fairly low, particularly when compared to the corresponding value for Cases A and C (Table 2).

Table 3 also provides values of the pressure drop in the system, $\Delta p_{\text{in-out}}$, which is about six times lower for the body-fitted design. This considerable discrepancy is not attributed to an insufficient mesh resolution, as refining the mesh to a level comparable to the body-fitted mesh only lowered $\Delta p_{\text{in-out}}$ by a factor of 1.4. It is rather explained by the smaller “effective” channel diameter³ of the porous design, resulting in higher velocities (as a result of mass conservation) and pressure losses. In fact, upon examination of the porous velocity solution in Fig. 9, one can observe that the $\tilde{\gamma} = 0.5$ isosurface does not accurately represent the effective channel wall position. The observed velocity field may also seem contradictory when considering the solid fraction distribution of Fig. 11, where transitions of γ from zero to one predominantly occur within one or two finite elements. The effective channel size is actually affected by both the Darcy friction force factor, C_α , and by the permeability penalty coefficient, P_α : a larger C_α (or lower P_α) results in a smaller effective channel diameter. On the one hand, increasing C_α increases the friction force where $\gamma > 0$ and, in particular, in the fluid boundary layer, which shrinks the channel size. On the other hand, a rise in P_α drives permeability values closer to α_{fluid} , resulting

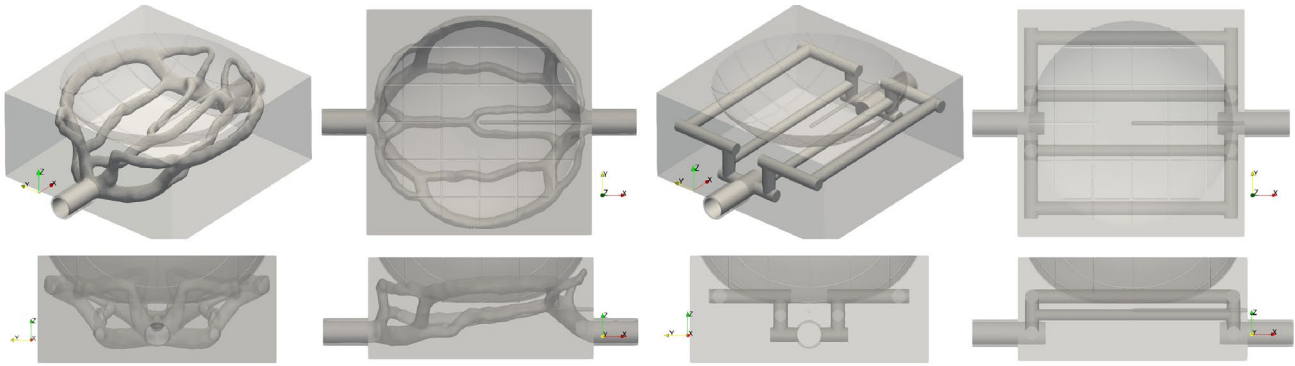


Fig. 12 Optimized (left) and straight (right) cooling channel designs considered in the experimental studies

in a reduction of the Darcy force contribution and a larger effective size.

By increasing both P_κ and P_α to 4×10^4 and solving for the same solid fraction distribution, the obtained $\Delta p_{\text{in-out}}$, \bar{T}_c , and σ_c values are now much closer to the body-fitted values, as noted in Table 3.

Lastly, the values of $P_\kappa = 4$ and $P_\alpha = 400$ used in the optimization were selected based on a trade-off between optimization problem stiffness reduction and accuracy of the temperature solutions. Emphasis was placed on the accuracy of the latter rather than on pressure losses. This prioritization aligns with the primary focus of this work, which is cooling channel design, and larger values of P_κ and P_α would have stiffened the optimization. Furthermore, the main objective of the pressure drop penalization, within our context, is to promote the generation of delineated channels rather than reaching a target value. If the objective was to constrain $\Delta p_{\text{in-out}}$ under some value, a different calibration approach would have been selected for the P_κ , P_α , and C_α values, and the continuation strategy may need to be revisited. Therefore, there is still room for improvement regarding hyper-parameter tuning in density-based optimizations, especially in multiphysics applications; trade-offs on accuracy and robustness are seemingly inevitable, as also pointed out by previous authors (Alexandersen et al. 2016).

3 Experimental studies

The main objective of the experimental studies is to validate the cooling channel design obtained through our topology optimization framework. More specifically, the goal is to verify that the generated channel configuration can be manufactured by LPBF and that the design efficiency is as expected. The main metrics of interest in this study are the heat extraction rate and the uniformity of the cavity temperature. Given the considerable challenge in imposing a constant heat flux on the cavity surface while monitoring

its temperature distribution, the experimental conditions are slightly different than the computational ones. As exposed in the following, the main difference lies in the consideration of transient conditions in the experiments. Although the cooling channels were designed for a steady state, we estimated that the proposed experimental time-dependent case is still relevant for the proof of concept objective.

3.1 Apparatus, instrumentation, and methodology

The two considered designs for validation are shown in Fig. 12. The first one, denoted as the “optimized” channel design, consists in the topology optimization solution for Case D (see Sect. 2.4), for which the body-fitted geometry was presented in Sect. 2.5. The second configuration, hereafter referred to as the “straight” channel design, is composed of circular channels connected in series and in parallel, so as to represent an efficient design that could be manufactured by conventional methods, i.e., straight-drilling combined with plugs. In particular, the flow is divided into four channels parallel to the x direction and of 6 mm (top two) and 5 mm (bottom two) diameter. The bottom channels were made smaller in order to increase the flow restriction in these sections, thus distributing the flow more evenly between the top and bottom segments. The minimal channel-to-cavity distance is about 2.5 mm (in accordance with the optimized

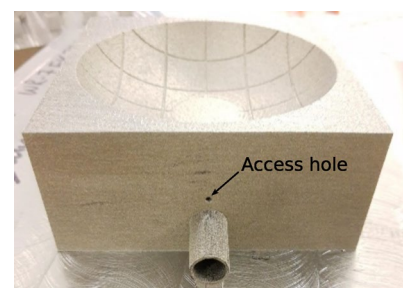
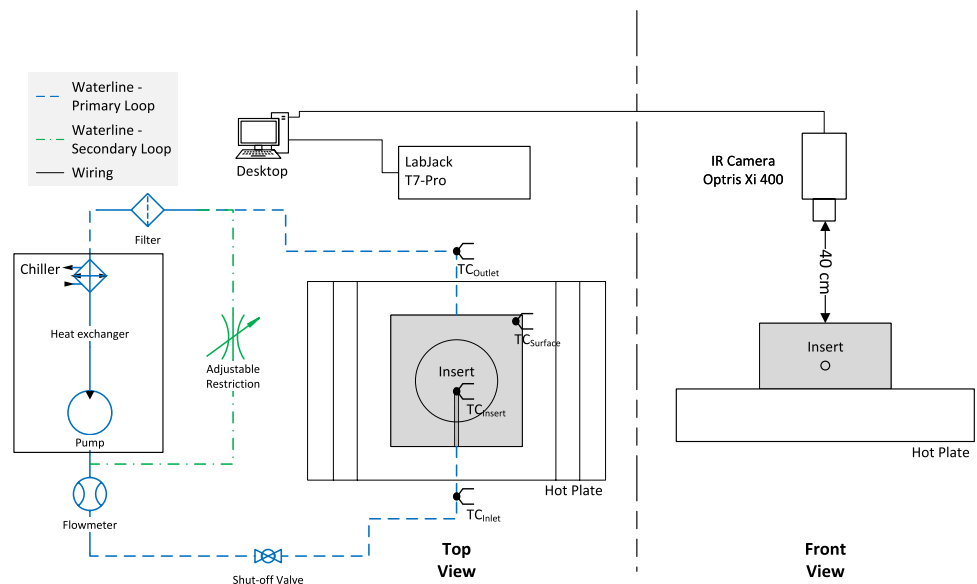


Fig. 13 Photograph of one of the inserts manufactured by LPBF

Fig. 14 Schematic diagram of the experimental apparatus

design) and is observed at mid-distance between the inlet and outlet. Following simulation-based design iterations and adjustments of the plug geometries, the fluid volume fraction, $1 - \bar{\gamma}$, reached 0.044, i.e., a value comparable to the optimized design volume fraction of 0.05. To mitigate any potential uncertainties (on e.g., the thermal properties of the material and the surface roughness of the channels) arising from the use of different manufacturing technologies, both designs are fabricated by Laser Powder Bed Fusion (LPBF), using a EOS M 290 printer and 18Ni-300 maraging steel powder. The result for one of the two inserts is shown in Fig. 13.

To characterize the cooling efficiency of both designs, the experimental apparatus shown schematically in Fig. 14 is utilized. The die insert is positioned on a laboratory hot plate, with the cavity facing upward. The top insert surface, including the cavity, is painted flat black in order to increase and regularize its emissivity (estimated to $\epsilon \approx 0.95$). A mineral wool sheet is loosely tightened around the insert and covers the four side walls. T-type thermocouples 0.318 cm in diameter are inserted in T-junctions located upstream of the inlet and downstream of the outlet ports. The tips are perpendicular to the flow streamwise direction and positioned at the tube centerline. Another thermocouple of the same type is inserted in the access hole (see Fig. 13) and monitors the temperature directly below the cavity center. An Optris Xi-400 infrared (IR) camera is placed approximately 40 cm above the insert in order to monitor the cavity surface temperature. The water circulation and thermal regulation are provided by a chiller (Polyscience LS51MX1A110C) and

Table 4 Reference temperatures, in °C, used in (26)

	Computations	Experiments
\bar{T}_{cool}	22	23.6
\bar{T}_0	60	57.9

Experimental values are computed based on the IR camera data

the flow rate is adjusted using a rotameter equipped with a metering valve. The thermocouples and camera signals are acquired at a one second interval through a data acquisition system (LabJack T7-Pro). In the context of this study, one will note that the primary function of the thermocouples is to qualitatively monitor the overall heating and cooling processes and to cross-validate the temperatures recorded by the IR camera.

The experimental procedure consists of two phases: a first stage where the insert is heated until some quasi-steady condition, followed by a cooling period. Phase one begins by powering the chiller, with a temperature setpoint of 22 °C. All valves are fully open until the setpoint is reached and steady. The flow rate is then set to 0.41 L/min, corresponding to $Re \approx 1000$. Next, the shut-off valve is closed, such that the water is directly recirculated to the chiller through the secondary flow loop; the hot plate is powered on and set to a surface temperature of 60 °C⁴; and the data acquisition is started. Following 35 min of heating, phase two is initiated by powering-off the hot plate and reopening the shut-off valve, thus allowing the water to circulate into the cooling channels. The experiment is ended after 15 min of cooling.

⁴ Due to the absence of insulation on the top surface (intended for visual access), a one degree Celsius variation was measured between the bottom and top regions of the cavity at the end of phase one.

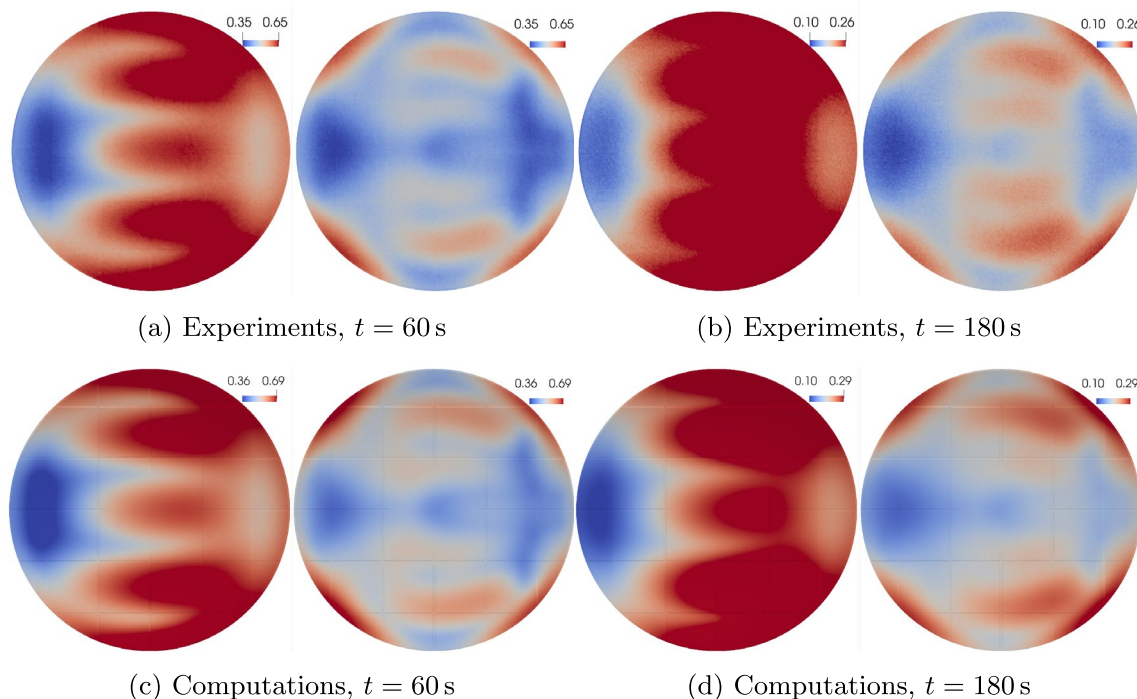


Fig. 15 Dimensionless temperature of the cavity at two instants of the cooling phase for the experiments (a–b) and computations (c–d); $t = 0$ s marks the phase start. The left and right plots of each subfig-

ure represent the results for the straight and optimized design, respectively. The flow is from left to right

3.2 Adjustment of the computational parameters

Additional computations are performed following slight modifications of the optimization conditions (exposed in Fig. 2) to align with the experiments. Only the cooling stage, i.e., phase two, is considered in the simulations. The heat flux on the cavity surface is replaced by an adiabatic condition; the inlet temperature is changed to 22 °C; and the initial temperature is set to 60 °C. For the optimized design, the body-fitted mesh of Sect. 2.5 is used, whereas a grid of same mesh density is utilized for the straight configuration.

For the considered Reynolds number of 1000, a steady-state solution is reached for u and p following a few tens of a second of simulation for the optimized channels. For the straight design, however, the steady state is never reached, likely attributable to the more aggressive changes in flow direction through the 90° bends. Hence, a time step value of 0.01 s is used for the straight channels computations to ensure convergence, while a value of 0.1 s proved to be adequate for the optimized design. Computations are performed for 500 s.

Radiation and natural convection from the top and cavity surfaces are neglected. This choice is justified due to the relatively low temperatures involved and the high level of convective heat transfer.

3.3 Results and discussion

The main metric of interest to validate the designs cooling efficiency is the surface temperature of the cavity, as this would be the location where, in a real application, material would be injected or formed. Comparative images of the experimental and computational cavity temperature distributions are shown in Fig. 15 at two instants during the cooling phase. The experimental results were extracted from the IR camera snapshots. Because of the slight differences in conditions between the experiments and computations, temperatures were made dimensionless using the following equations:

$$\bar{T}_c^* = \frac{\bar{T}_c - \bar{T}_{cool}}{\bar{T}_0 - \bar{T}_{cool}}, \tag{25}$$

$$\sigma_c^* = \frac{\sigma_c}{\bar{T}_0 - \bar{T}_{cool}}, \tag{26}$$

where \bar{T}_0 and \bar{T}_{cool} denote the initial ($t = 0$) and final (steady state) average cavity temperature, respectively, which are provided in Table 4. The discrepancies for \bar{T}_0 and \bar{T}_{cool} are, respectively, attributed to the observed vertical temperature variation of the inserts in the experiments (see Sect. 3.1),

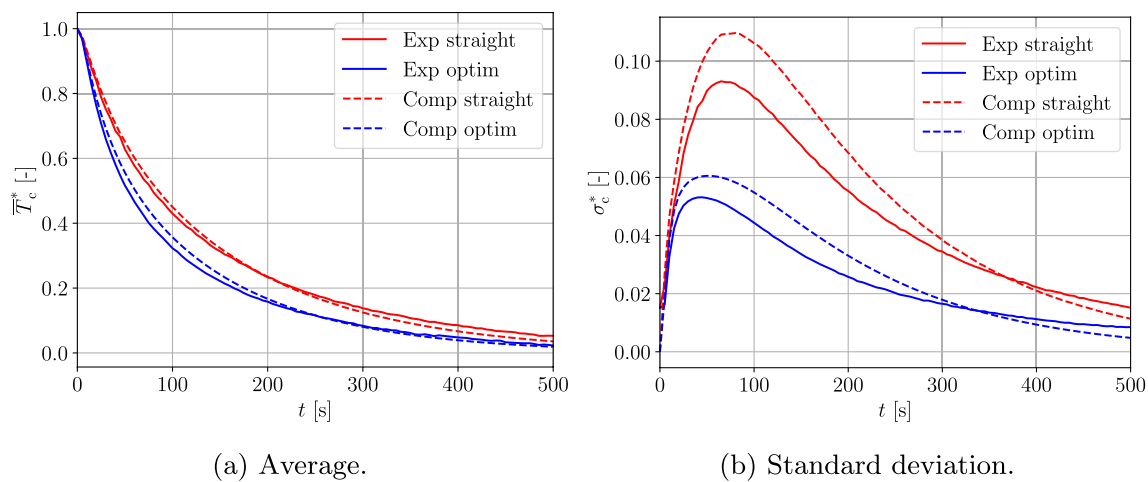


Fig. 16 Cavity temperature with time—experiments and computations

and to the relative uncertainty of the IR camera, which is larger for temperatures close to ambient.

A first prominent observation from the figure is the remarkable match between the results from experiments and computations, especially for $t = 60$ s. The colder and hotter spots are indeed well predicted by the simulations, both in terms of location and magnitude. A second observation is the much lower temperature variation for the optimized design, thanks to the consideration of the temperature STD in the optimization. In particular, for the straight design, the cavity is much cooler close to the inlet (leftmost region). In Fig. 16, the average and STD temperatures of the cavity, \bar{T}_c^* and σ_c^* , are plotted over time. It is observed that the maximum σ_c^* occurs for $t \approx 60$ s for both the straight and optimized designs, and that this value is 43% lower for the optimized channels in the experiments (45% in the computations). The overall cooling, in an average sense, is also faster with the optimized design, as depicted by Fig. 16a. Indeed, throughout the test duration, the straight channel design maintains a higher cavity temperature. These results further validate our topology optimization framework and demonstrate that the generated designs can be manufactured and provide the expected superior cooling efficiency.

4 Conclusion

In this work, a density-based topology optimization approach for the design of additively manufactured cooling channels is presented. The strategy includes a modified projected-perimeter overhang constraint to ensure AM manufacturability and a penalization on the temperature standard deviation to promote temperature uniformity. We show that employing the filtered design variable, as opposed

to the physical design variable, in the projected-perimeter formulation leads to a more efficient design and necessitates a less aggressive target value. Optimizations are performed in a cuboid geometry featuring a heated hemispherical cavity, with and without the overhang constraint and STD penalization. The activation of the former promotes the formation of channels with a teardrop-shaped cross section, while the use of the latter mitigates both over- and under-cooled regions through local adjustment of the channel-to-cavity distance, which in particular inhibits channels from forming too close to the cavity.

The optimized design obtained by considering both the overhang constraint and STD penalization is validated computationally and experimentally. First, a body-fitted mesh is generated and the solutions for temperature and velocity are obtained using a traditional conjugate heat transfer solver. The results indicate a good match between the porous and body-fitted temperature distributions, but reveals a significant discrepancy on the system pressure losses, which is explained by an inadequate tuning of the Darcy friction force and permeability penalty parameters. Nonetheless, within the present optimization context

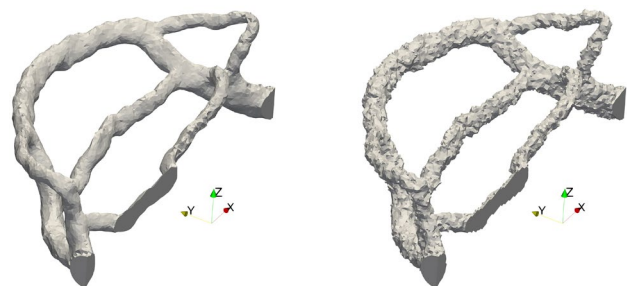


Fig. 17 Case D final design, as represented by the $\tilde{\gamma} \leq 0.5$ (left) and $\gamma \leq 0.5$ (right) clip, respectively

Table 5 Results for two body-fitted meshes, based on the final design of Case D

Case	\bar{T}_c (C)	σ_c (C)	Δp_{in-out} (Pa)
$\gamma = 0.5$	169.2	5.02	30.8
$\tilde{\gamma} = 0.5$	166.9	5.34	27.4

emphasizing heat transfer efficiency, the specific pressure loss value is not of central importance. Next, experiments are performed in order to complete the validation of our approach, namely to confirm both the manufacturability of the generated design using AM and its alignment with expected efficiency levels. Two inserts are fabricated by LPBF: one with the optimized cooling lines, and another with a straight-drilled channel configuration. Our demonstration reveals a remarkable alignment between the experimental temperature field and computational results, and

that the optimized design leads to a superior heat transfer rate, along with a 43% decrease on the temperature STD of the cavity surface, when compared to the straight channels design.

Although optimizations and experiments were conducted under distinct conditions (steady state and time-dependent, respectively), it is noteworthy that the optimized channels geometry exhibits excellent performance. While this observation holds for the specific problem at hand, its applicability to all conditions is improbable; the consideration of transient conditions within the optimization is deferred to future research. Finally, another planned investigation involves assessing the performance of the current optimized channels design, initially designed for laminar flow, under turbulent conditions.

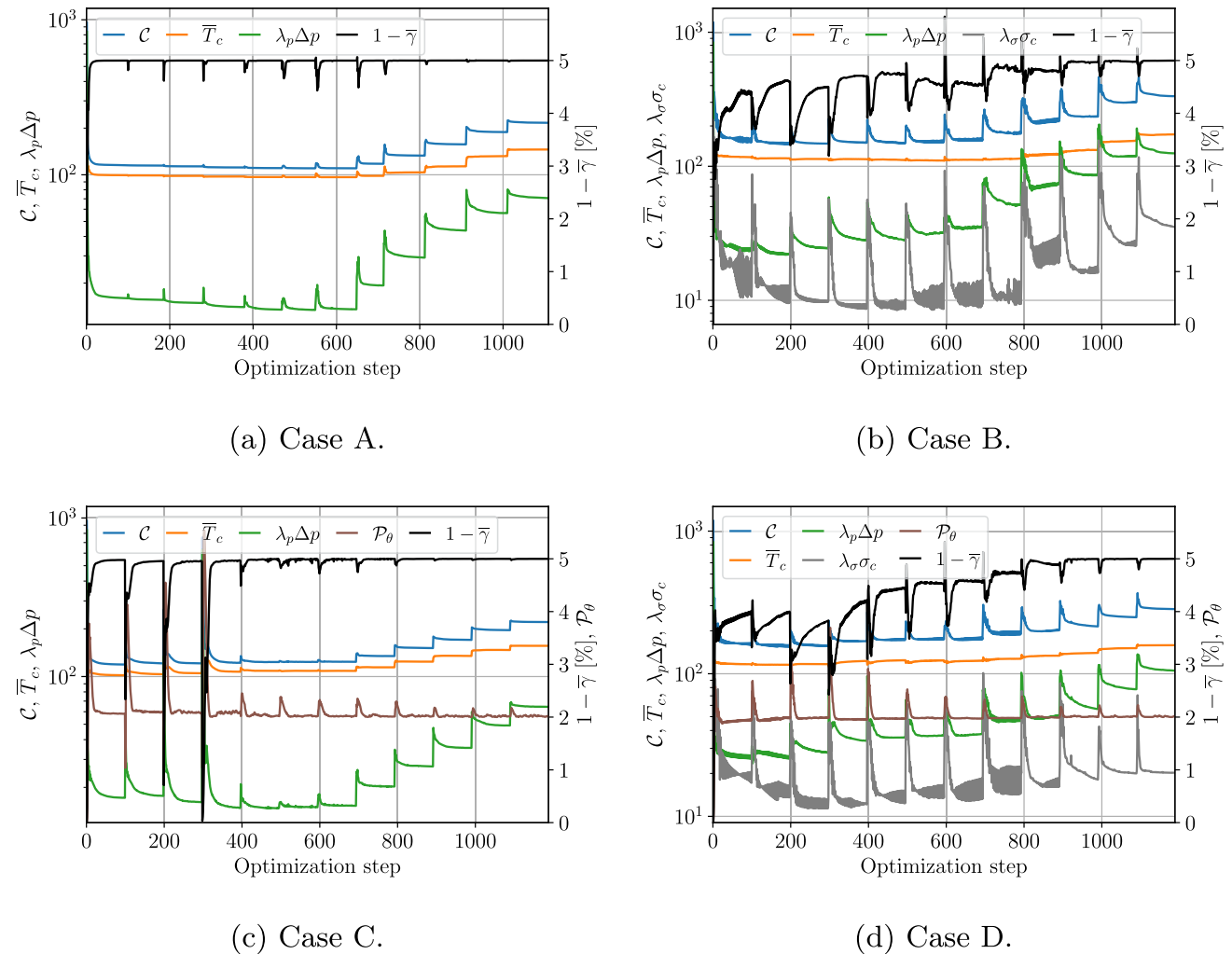


Fig. 18 Cost function evolution for Cases A–D

Appendix A: Performance comparison of the $\gamma = 0.5$ and $\tilde{\gamma} = 0.5$ designs

This section investigates the effect of using the filtered instead of the physical design variable when generating the body-fitted mesh. Two meshes are generated using the implicit domain meshing algorithm of the mmg3d library (Dapogny et al. 2014), i.e., following a splitting of the optimization mesh on $\gamma = 0.5$ for the first mesh, and on $\tilde{\gamma} = 0.5$ for the second one. The γ and $\tilde{\gamma}$ distributions of the Case D final design are utilized for this exercise. Then, the Navier–Stokes and energy conservation equations are solved using the body-fitted solver on the two meshes for the same conditions as in the optimization case (see Sect. 2.4.1). First, one can note that, besides the significantly higher surface roughness of the $\gamma = 0.5$ design, both geometries closely resemble each other, as illustrated in Fig. 17. The results listed in Table 5 further show that the pressure losses and the average cavity temperature are only 11.0 and 1.4% higher, while σ_c is reduced by 6.7%, when compared to the $\tilde{\gamma} = 0.5$ design.

Similar observations were noted for other cases obtained with the proposed methodology (see Sect. 2.3.2). The good agreement between the $\gamma = 0.5$ and $\tilde{\gamma} = 0.5$ isosurfaces can be mainly attributed to the crispness of the γ distributions. The level of discreteness of the final design of Cases A–F was at most 3.4%, as indicated in Table 2.

Appendix B: Cost function series for Cases A–D

The evolution of the cost function, constraints, and penalization terms can be tracked in Fig. 18 for the different optimization cases. Let us recall that the optimizations are spanned by 12 loops and follow the continuation strategy presented in Sect. 2.3.2. One can first observe for Case A that, within each loop, the cost function decreases smoothly with iterations and the volume constraint target is reached. For loops 8 to 12, the observed series of steps of the final \mathcal{C} value is explained by the rise of C_α . When the STD penalization is used (Cases B and D), we note the presence of oscillations on σ_c . Furthermore, the optimizer does not utilize all the allowed volume of fluid in loops 1–9. However, as C_α is increased, and thanks to the gradual rise of the hyper-parameters, the oscillations eventually vanish and the target fluid volume is progressively reached. The exploration of alternative formulations to the STD penalization, which could mitigate the observed oscillations and improve convergence, is left for future work.

Appendix C: Expressions of the sensitivity analysis

The adjoint Eqs. (22) and (23), right-hand side components are evaluated as follows:

$$\begin{aligned} \frac{\partial \mathcal{C}}{\partial T_i} &= \frac{\partial \bar{T}_c}{\partial T_i} + \lambda_\sigma \frac{\partial \sigma_c}{\partial T_i} \\ &= \frac{1}{A_c} \int_{\Gamma_c} \phi_i \, d\Gamma + \frac{\lambda_\sigma}{A_c \sigma_c} \left[\int_{\Gamma_c} T_i \phi_i \, d\Gamma - \bar{T}_c \int_{\Gamma_c} \phi_i \, d\Gamma \right], \end{aligned} \tag{27}$$

$$\begin{aligned} \frac{\partial \mathcal{C}}{\partial U_i^{NS}} &= \frac{\partial}{\partial p_i} (\lambda_p \Delta p_{in-out}) \\ &= \frac{\lambda_p}{A_{in}} \int_{\Gamma_{in}} \phi_i \, d\Gamma, \end{aligned} \tag{28}$$

with

$$A_{\square} = \int_{\Gamma_{\square}} d\Gamma, \quad \bar{T}_c = \frac{1}{A_c} \int_{\Gamma_c} T_i \phi_i \, d\Gamma, \tag{29}$$

where ϕ_i is the finite element interpolation function for the degree of freedom i and \square denotes a specific boundary.

Funding Open access funding provided by National Research Council Canada library. This work was partially supported by the National Research Council of Canada METALtec industrial research group, as well as by the Office of Energy Research and Development of Canada (grant NRC-20-09) and by the Centre Québécois de Recherche et de Développement de l’Aluminium (grant CNRC1058).

Declarations

Conflict of interest The authors have no relevant financial or non-financial interests to disclose.

Replication of results Data sets generated during the current study were generated using NRC’s proprietary software and are available from the corresponding author on reasonable request.

Open Access This article is licensed under a Creative Commons Attribution 4.0 International License, which permits use, sharing, adaptation, distribution and reproduction in any medium or format, as long as you give appropriate credit to the original author(s) and the source, provide a link to the Creative Commons licence, and indicate if changes were made. The images or other third party material in this article are included in the article’s Creative Commons licence, unless indicated otherwise in a credit line to the material. If material is not included in the article’s Creative Commons licence and your intended use is not permitted by statutory regulation or exceeds the permitted use, you will need to obtain permission directly from the copyright holder. To view a copy of this licence, visit <http://creativecommons.org/licenses/by/4.0/>.

References

- Alexandersen J, Sigmund O, Aage N (2016) Large scale three-dimensional topology optimisation of heat sinks cooled by natural convection. *Int J Heat Mass Transf* 100:876–891. <https://doi.org/10.1016/j.ijheatmasstransfer.2016.05.013>
- Alexandersen J, Sigmund O, Meyer KE, Lazarov BS (2018) Design of passive coolers for light-emitting diode lamps using topology optimisation. *Int J Heat Mass Transf* 122:138–149. <https://doi.org/10.1016/j.ijheatmasstransfer.2018.01.103>
- Allaire G, Dapogny C, Estevez R, Faure A, Michailidis G (2017) Structural optimization under overhang constraints imposed by additive manufacturing technologies. *J Comput Phys* 351:295–328. <https://doi.org/10.1016/j.jcp.2017.09.041>
- Audet M, Hétu JF, Ilinca F (2008) DFEMwork: a parallel computing framework for material processing. In: 5th NRC symposium on computational fluid dynamics and multi-scale modeling. Canada, Ottawa, pp 1–10
- Behrou R, Kirsch K, Ranjan R, Guest JK (2022) Topology optimization of additively manufactured fluidic components free of internal support structures. *Comput Methods Appl Mech Eng* 389:114270. <https://doi.org/10.1016/j.cma.2021.114270>
- Borrvall T, Petersson J (2003) Topology optimization of fluids in Stokes flow. *Int J Numer Methods Fluids* 41(1):77–107. <https://doi.org/10.1002/flid.426>
- Bruns TE, Tortorelli DA (2001) Topology optimization of non-linear elastic structures and compliant mechanisms. *Comput Methods Appl Mech Eng* 190(26):3443–3459. [https://doi.org/10.1016/S0045-7825\(00\)00278-4](https://doi.org/10.1016/S0045-7825(00)00278-4)
- Çalışkan Cİ, Koca A, Özer G, Akbal Ö, Bakır S (2023) Efficiency comparison of conformal cooling channels produced by additive and subtractive manufacturing in automotive industry plastic injection moulds: a hybrid application. *Int J Adv Manuf Technol* 126(9):4419–4437. <https://doi.org/10.1007/s00170-023-11389-y>
- Chowdhury S, Yadaiah N, Prakash C, Ramakrishna S, Dixit S, Gupta LR, Buddhi D (2022) Laser powder bed fusion: a state-of-the-art review of the technology, materials, properties & defects, and numerical modelling. *J Market Res* 20:2109–2172. <https://doi.org/10.1016/j.jmrt.2022.07.121>
- Cignoni P, Callieri M, Corsini M, Dellepiane M, Ganovelli F, Ranzuglia G (2008) MeshLab: an open-source mesh processing tool. In: Eurographics Italian chapter conference p 8 pages. <https://doi.org/10.2312/LOCALCHAPTEREVENTS/ITALCHAP/ITALIANCHAPCONF2008/129-136>
- Covarrubias EE, Eshraghi M (2018) Effect of build angle on surface properties of Nickel superalloys processed by selective laser melting. *JOM* 70(3):336–342. <https://doi.org/10.1007/s11837-017-2706-y>
- Dapogny C, Dobrzynski C, Frey P (2014) Three-dimensional adaptive domain remeshing, implicit domain meshing, and applications to free and moving boundary problems. *J Comput Phys* 262:358–378. <https://doi.org/10.1016/j.jcp.2014.01.005>
- Dede EM (2009) Multiphysics topology optimization of heat transfer and fluid flow systems. In: Proceedings of the COMSOL conference 2009 Boston, p 7
- Dilgen SB, Dilgen CB, Fuhrman DR, Sigmund O, Lazarov BS (2018) Density based topology optimization of turbulent flow heat transfer systems. *Struct Multidiscip Optim* 57(5):1905–1918. <https://doi.org/10.1007/s00158-018-1967-6>
- Feng S, Kamat AM, Pei Y (2021) Design and fabrication of conformal cooling channels in molds: review and progress updates. *Int J Heat Mass Transf* 171:121082. <https://doi.org/10.1016/j.ijheatmasstransfer.2021.121082>
- Garaigordobil A, Ansola R, Veguería E, Fernandez I (2019) Overhang constraint for topology optimization of self-supported compliant mechanisms considering additive manufacturing. *Comput Aided Des* 109:33–48. <https://doi.org/10.1016/j.cad.2018.12.006>
- Gaynor AT, Guest JK (2016) Topology optimization considering overhang constraints: eliminating sacrificial support material in additive manufacturing through design. *Struct Multidiscip Optim* 54(5):1157–1172. <https://doi.org/10.1007/s00158-016-1551-x>
- Geuzaine C, Remacle JF (2009) Gmsh: a 3-D finite element mesh generator with built-in pre- and post-processing facilities. *Int J Numer Methods Eng* 79(11):1309–1331. <https://doi.org/10.1002/nme.2579>
- Ibhaddode O, Zhang Z, Sixt J, Nsiempba KM, Orakwe J, Martinez-Marchese A, Ero O, Shahabadi SI, Bonakdar A, Toyserkani E (2023) Topology optimization for metal additive manufacturing: current trends, challenges, and future outlook. *Virtual Phys Prototyp* 18(1):e2181192. <https://doi.org/10.1080/17452759.2023.2181192>
- Jahan S, Wu T, Shin Y, Tovar A, El-Mounayri H (2019) Thermo-fluid topology optimization and experimental study of conformal cooling channels for 3D printed plastic injection molds. *Proc Manuf* 34:631–639. <https://doi.org/10.1016/j.promfg.2019.06.120>
- Kanbur BB, Suping S, Duan F (2020) Design and optimization of conformal cooling channels for injection molding: a review. *Int J Adv Manuf Technol* 106(7):3253–3271. <https://doi.org/10.1007/s00170-019-04697-9>
- Koga AA, Lopes EC, Nova HF, De Lima CR, Silva EC (2013) Development of heat sink device by using topology optimization. *Int J Heat Mass Transf* 64:759–772. <https://doi.org/10.1016/j.ijheatmasstransfer.2013.05.007>
- Langelaar M (2017) An additive manufacturing filter for topology optimization of print-ready designs. *Struct Multidiscip Optim* 55(3):871–883. <https://doi.org/10.1007/s00158-016-1522-2>
- Li Z, Wang X, Gu J, Ruan S, Shen C, Lyu Y, Zhao Y (2018) Topology optimization for the design of conformal cooling system in thin-wall injection molding based on BEM. *Int J Adv Manuf Technol* 94(1):1041–1059. <https://doi.org/10.1007/s00170-017-0901-1>
- Li H, Ding X, Jing D, Xiong M, Meng F (2019a) Experimental and numerical investigation of liquid-cooled heat sinks designed by topology optimization. *Int J Therm Sci* 146:106065. <https://doi.org/10.1016/j.ijthermalsci.2019.106065>
- Li H, Ding X, Meng F, Jing D, Xiong M (2019b) Optimal design and thermal modelling for liquid-cooled heat sink based on multi-objective topology optimization: an experimental and numerical study. *Int J Heat Mass Transf* 144:118638. <https://doi.org/10.1016/j.ijheatmasstransfer.2019.118638>
- Li H, Kondoh T, Jolivet P, Furuta K, Yamada T, Zhu B, Zhang H, Izui K, Nishiwaki S (2022) Optimum design and thermal modeling for 2D and 3D natural convection problems incorporating level set-based topology optimization with body-fitted mesh. *Int J Numer Methods Eng* 123(9):1954–1990. <https://doi.org/10.1002/nme.6923>
- Liu J, Gaynor AT, Chen S, Kang Z, Suresh K, Takezawa A, Li L, Kato J, Tang J, Wang CC, Cheng L (2018) Current and future trends in topology optimization for additive manufacturing. *Struct Multidiscip Optim* 57(6):2457–2483. <https://doi.org/10.1007/s00158-018-1994-3>
- Matsumori T, Kondoh T, Kawamoto A, Nomura T (2013) Topology optimization for fluid-thermal interaction problems under constant input power. *Struct Multidiscip Optim* 47(4):571–581. <https://doi.org/10.1007/s00158-013-0887-8>
- Mazur M, Brincat P, Leary M, Brandt M (2017) Numerical and experimental evaluation of a conformally cooled H13 steel injection mould manufactured with selective laser melting. *Int J Adv Manuf Technol* 93(1):881–900. <https://doi.org/10.1007/s00170-017-0426-7>
- Miki T (2023) Self-support topology optimization considering distortion for metal additive manufacturing. *Comput Methods*

- Appl Mech Eng 404:115821. <https://doi.org/10.1016/j.cma.2022.115821>
- Navah F, Lamarche-Gagnon M \acute{E} , Ilinca F (2024) Thermofluid topology optimization for cooling channel design. *Appl Therm Eng* 236:121317. <https://doi.org/10.1016/j.applthermaleng.2023.121317>
- Navah F, Lamarche-Gagnon M \acute{E} , Ilinca F, Audet M, Molavi-Zarandi M, Raymond V (2022) Development of a topology optimization framework for cooling channel design in die casting molds. In: Proceedings of the ASME 2021, international mechanical engineering congress and exposition. American Society of Mechanical Engineers Digital Collection. <https://doi.org/10.1115/IMECE2021-73363>
- Ozgu \acute{c} S, Teague TF, Pan L, Weibel JA (2023) Experimental study of topology optimized, additively manufactured microchannel heat sinks designed using a homogenization approach. *Int J Heat Mass Transf* 209:124108. <https://doi.org/10.1016/j.ijheatmasstransfer.2023.124108>
- Pollini N, Sigmund O, Andreassen CS, Alexandersen J (2020) A “poor man’s” approach for high-resolution three-dimensional topology design for natural convection problems. *Adv Eng Softw* 140:102736. <https://doi.org/10.1016/j.advengsoft.2019.102736>
- Qian X (2017) Undercut and overhang angle control in topology optimization: a density gradient based integral approach. *Int J Numer Methods Eng* 111(3):247–272. <https://doi.org/10.1002/nme.5461>
- Qian X, Dede EM (2016) Topology optimization of a coupled thermal-fluid system under a tangential thermal gradient constraint. *Struct Multidiscip Optim* 54(3):531–551. <https://doi.org/10.1007/s00158-016-1421-6>
- Qian S, Lou S, Ge C, Wang W, Tian X, Cai Y (2022) The influence of temperature dependent fluid properties on topology optimization of conjugate heat transfer. *Int J Therm Sci* 173:107424. <https://doi.org/10.1016/j.ijthermalsci.2021.107424>
- Sigmund O (2007) Morphology-based black and white filters for topology optimization. *Struct Multidiscip Optim* 33(4–5):401–424. <https://doi.org/10.1007/s00158-006-0087-x>
- Sigmund O, Maute K (2013) Topology optimization approaches: a comparative review. *Struct Multidiscip Optim* 48(6):1031–1055. <https://doi.org/10.1007/s00158-013-0978-6>
- Stolpe M, Svanberg K (2001a) An alternative interpolation scheme for minimum compliance topology optimization. *Struct Multidiscip Optim* 22(2):116–124. <https://doi.org/10.1007/s001580100129>
- Stolpe M, Svanberg K (2001b) On the trajectories of penalization methods for topology optimization. *Struct Multidiscip Optim* 21(2):128–139. <https://doi.org/10.1007/s001580050177>
- Sun S, Rankouhi B, Thoma DJ, Cheadle MJ, Maples GD, Anderson MH, Nellis G, Qian X (2024) Topology optimization, additive manufacturing and thermohydraulic testing of heat sinks. *Int J Heat Mass Transf* 224:125281. <https://doi.org/10.1016/j.ijheatmasstransfer.2024.125281>
- Svanberg K (1987) The method of moving asymptotes—a new method for structural optimization. *Int J Numer Methods Eng* 24(2):359–373. <https://doi.org/10.1002/nme.1620240207>
- Tezduyar TE, Mittal S, Ray SE, Shih R (1992) Incompressible flow computations with stabilized bilinear and linear equal-order-interpolation velocity-pressure elements. *Comput Methods Appl Mech Eng* 95(2):221–242. [https://doi.org/10.1016/0045-7825\(92\)90141-6](https://doi.org/10.1016/0045-7825(92)90141-6)
- van de Ven E, Maas R, Ayas C, Langelaar M, van Keulen F (2018) Continuous front propagation-based overhang control for topology optimization with additive manufacturing. *Struct Multidiscip Optim* 57(5):2075–2091. <https://doi.org/10.1007/s00158-017-1880-4>
- Van Dijk NP, Maute K, Langelaar M, Van Keulen F (2013) Level-set methods for structural topology optimization: a review. *Struct Multidiscip Optim* 48(3):437–472. <https://doi.org/10.1007/s00158-013-0912-y>
- Wang F, Lazarov BS, Sigmund O (2011) On projection methods, convergence and robust formulations in topology optimization. *Struct Multidiscip Optim* 43(6):767–784. <https://doi.org/10.1007/s00158-010-0602-y>
- Wang Y, Gao J, Kang Z (2018) Level set-based topology optimization with overhang constraint: towards support-free additive manufacturing. *Comput Methods Appl Mech Eng* 339:591–614. <https://doi.org/10.1016/j.cma.2018.04.040>
- Wang Y, Wang J, Liu X (2022) Topology optimization design of microchannel heat sink by considering the coupling of fluid-solid and heat transfer. *Energies* 15(23):8827. <https://doi.org/10.3390/en15238827>
- Wang H, Wang Z, Zhu J, Zhang W, Ming P (2023) Thermal-fluid-structural topology optimization of coolant channels in a proton exchange membrane fuel cell. *Int Commun Heat Mass Transf* 142:106648. <https://doi.org/10.1016/j.icheatmasstransfer.2023.106648>
- Wu J, Sigmund O, Groen JP (2021) Topology optimization of multi-scale structures: a review. *Struct Multidiscip Optim* 63(3):1455–1480. <https://doi.org/10.1007/s00158-021-02881-8>
- Yaji K, Yamada T, Kubo S, Izui K, Nishiwaki S (2015) A topology optimization method for a coupled thermal-fluid problem using level set boundary expressions. *Int J Heat Mass Transf* 81:878–888. <https://doi.org/10.1016/j.ijheatmasstransfer.2014.11.005>
- Yaji K, Yamada T, Yoshino M, Matsumoto T, Izui K, Nishiwaki S (2016) Topology optimization in thermal-fluid flow using the lattice Boltzmann method. *J Comput Phys* 307:355–377. <https://doi.org/10.1016/j.jcp.2015.12.008>
- Yu M, Ruan S, Gu J, Ren M, Li Z, Wang X, Shen C (2020) Three-dimensional topology optimization of thermal-fluid-structural problems for cooling system design. *Struct Multidiscip Optim* 62(6):3347–3366. <https://doi.org/10.1007/s00158-020-02731-z>
- Zhan S, Cheng Z, Yin Y, Yu C, Zhao C (2023) Effect of inlet and outlet positions on heat dissipation performance of lithium-ion battery cold plates: an analysis based on topology optimization. *Int J Heat Mass Transf* 215:124436. <https://doi.org/10.1016/j.ijheatmasstransfer.2023.124436>
- Zhang Y, Liu S (2008) The optimization model of the heat conduction structure. *Prog Nat Sci* 18(6):665–670. <https://doi.org/10.1016/j.pnsc.2008.01.010>
- Zhou J, Lu M, Zhao Q, Li Q, Chen X (2024) Topologically optimized manifold microchannel heat sink with extreme cooling performance for high heat flux cooling of electronics. *Appl Therm Eng* 241:122426. <https://doi.org/10.1016/j.applthermaleng.2024.122426>
- Zhu J, Zhou H, Wang C, Zhou L, Yuan S, Zhang W (2021) A review of topology optimization for additive manufacturing: status and challenges. *Chin J Aeronaut* 34(1):91–110. <https://doi.org/10.1016/j.cja.2020.09.020>

Publisher's Note Springer Nature remains neutral with regard to jurisdictional claims in published maps and institutional affiliations.